Influence of the configuration of elastic and dissipative elements on the energy harvesting efficiency of a tunnel effect energy harvester

Jerzy MARGIELEWICZ[1], Damian GĄSKA[1], Grzegorz LITAK[2], Daniil YURCHENKO[3], Piotr WOLSZCZAK[2], Andrzej DYMAREK[4], Tomasz DZITKOWSKI[4]

[1]*Silesian University of Technology, Faculty of Transport and Aviation Engineering, 40-019 Katowice, Poland*

[2]*Lublin University of Technology, Faculty of Mechanical Engineering, 20-618 Lublin, Poland*

[3]*University of Southampton, Institute of Sound and Vibration Research, Southampton,* SO17 1BJ*, UK*

[4]*Silesian University of Technology, Faculty of Mechanical Engineering, 41-100 Gliwice, Poland*

Corresponding author

Damian GĄSKA

Silesian University of Technology, Faculty of Transport and Aviation Engineering, Krasińskiego 8, Katowice 40-019, Poland, damian.gaska@polsl.pl

Influence of the configuration of elastic and dissipative elements on the energy harvesting efficiency of a tunnel effect energy harvester

Abstract: Paper presents computer simulations conducted to study the influence of the configuration of an energy harvesting system with tunnel mechanical characteristics in terms of its energy generation efficiency. In this context, numerical simulation experiments were carried out to assess the impact of physical properties and initial conditions on the occurrence of coexisting solutions and its energy efficiency. Chaotic motion zones were identified on the basis of Lyapunov exponent. To be able to choose the best solution in terms of energy efficiency, studies on the use of impulse excitation to change the orbit of the solution were also presented. Results show that modifying the energy harvesting system design with an impulse excitation subsystem can significantly improve (up to tenfold) the amount of energy harvested from vibrating mechanical devices.

Keywords: nonlinear dynamics, coexisting solutions, energy efficiency, basins of attraction, Lyapunov exponent

Highlights

A new energy harvesting system has been designed (TEEH).

The parameters' domains have been identified where the optimal energy harvesting is achieved.

The method of impulse excitation to change the unfavorable orbits is developed.

Basins of attraction of coexisting solutions are identified.

1. Introduction

In the last 20 years, we have witnessed the rapid development of all fields of science related to counteracting the impact of climate change. There are new solutions, both theoretical and practical, aimed at generating and implementing efficient usage of energy without negatively impacting the environment. One of these fields of science that has been intensively developing in particularly is energy harvesting [1,2], focused on generating

energy from phenomena encountered in the natural and built environment, such as mechanical vibrations, air flow, temperature gradient and others to power autonomic sensors in the distributed monitoring systems.

The energy efficiency of energy harvesting systems is currently low, but they can power simple measurement systems, powering, for example, three-axis accelerometers and wireless data transmission systems. It seems that more and more electronic devices and sensors will be powered in this way in the future [3]. Most of the energy harvesting solutions involve energy obtained from mechanical vibrations, which can be transformed through various transducers, such as piezoelectric [4,5], electrostatic [6], or electromagnetic [7]; however, significant number of scientific works are also concerned with energy harvesting from air flow [1,8–10] in which it is important to achieve a high efficiency under low operational wind speed by vortex-induced and galloping oscillations to harvest energy from a flow field [11,12].

A typical design of systems for harvesting energy from mechanical vibrations consists of a flexible cantilever beam with piezoelectric transducersattached. This design solution is then optimized in various ways introducing nonlinearity and, thus, enabling energy generation over a wide frequency spectrum of the excitation source [13]. Typical additional elements that introduce nonlinearities are magnets [14–17]. In addition, mechanical or electrical coupling of several beams [18,19] and systems based on single [20] or double pendulums [21,22] have been used. Each of the above-mentioned design solutions has certain limitations, the most important and common of which is a minimum level of energy from the external excitation, which is required to overcome local potential barriers to achive highorbit solutions. These limitations can be avoided by design solutions where the energy potential is characterized by appropriately-connected elastic and dissipative elements with a variable configuration [23]. A tunnel effect energy harvester

(TEEH), which is the subject of this publication, is an extension and generalization of the QZEH (quasi-zero energy harvester) structure presented in ref. [24]. We used this name due to the similarity of the mechanical characteristics of the tested system to the current-voltage characteristics of the tunnel diode.

Another interesting feature of nonlinear energy harvesters is the identification of their best efficiency, which requires time-consuming numerical experiments. Published research [24] indicates that periodic solutions, which can be established over a long time period, are characterized by the highest energy harvesting efficiency. Finding steady-state periodic solutions becomes an important problem because, in nonlinear systems, there are multiple stable periodic solutions, unstable periodic solutions and transient chaotic solutions [25]. From a theoretical point of view, nonlinear dynamics have numerical tools to control chaos [26]. However, from the energy harvesting point of view such studies should assess whether the minimum amount of energy supplied to the control system does not exceed that harvested by the harvester from vibrations. Zhang et al. [27] proposed a high-energy sliding mode control method through rotatable magnets actuated by a micro-motor. Wang and Liao [7] also proposed a load perturbation method to attain a high-energy orbit in a nonlinear energy harvester. Huang et al. proposed a systematic adjustment strategy by a slow structural characteristics matching technique, an extra energy impact technique, or a combination of these two [28]. The orbit jump concept using the synchronized switch stiffness control technique in nonlinear energy harvesters was presented by Yan et al. [29]. Similar methods that can change the orbit of the solution to one with a greater energy generation efficiency were introduced in refs. [30–33].

In this paper, a new energy harvesting system (TEEH) with identified coexisting solutions and an alternative method of influencing the nature of the solution is proposed. The

orbit of the solution can be changed by an external impulse imposed with the characteristics defined at a strictly-defined time instant. The obtained results provide an incentive to conduct research to design an external impulse excitation system, enabling a shift to solutions with greater energy harvesting efficiencies.

The paper has the following structure. Section 2 presents the formulation of the mathematical model of the analyzed energy harvesting system along with the identification of the mechanical characteristics. Section 3 presents the results of model tests with particular emphasis on the identification of coexisting solutions and their impact on the efficiency of energy harvesting. Section 4 presents the influence of impulse disturbance on the ability to harvest energy together with a proposal of a special IED diagram for visualization of the possibility of changing the solution to a more effective one.

2. Formulation of the mathematical model

The subject of this research is the TEEH system, in which the potential barrier was defined by using three elastic elements (Fig. 1). The test system assumed a symmetrical structure of connected elastic elements, which were attached at points *A, B,* and *C* to the non-deformable *IV* frame. Through bolt *III*, the system was rigidly attached to the vibrating machine component. Piezoelectrics were glued to the flat surfaces of flexible beam *I*, which, under the influence of dynamic external action, undergoes elastic deformation. The beam deformation lead to electric charge generated and transmitted through the piezoelectric electrodes *II*. Furthermore, during modeling tests, it was assumed that the inertial element *m*, mounted at the free end of the beam, could move along a straight line, the direction of which was determined by the axis of the main spring c_1. At the same time, this assumption determines the appropriate design solution, which is not the subject of this paper.

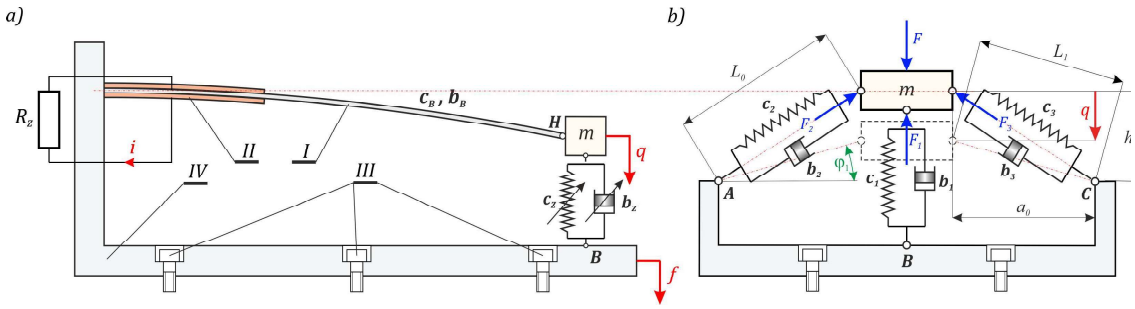

Fig. 1. Energy harvesting system with tunnel mechanical characteristics. a) phenomenological model, b) schematic diagram of the configuration of elastic and dissipative elements. A, B, C - joints of elastic elements to a rigid frame, H - mass *m* joint with a flexible beam

From the construction point of view, the considered system differs in the angular orientation of the compensation springs from the system with quasi-zero stiffness QZEH. In the *QZEH* system, the compensation springs c_2 and c_3, had a horizontal configuration, i.e., their axes were oriented parallel to the axis of the flexible beam. However, in the *TEEH* system, at static equilibrium, these springs were angularly oriented (angle φ_1 , Fig. 1b) with respect to the flexible beam *I*. This relatively subtle difference played an important role in the shape of the system's potential barrier. During the numerical experiments, it was assumed that the stiffnesses of the compensation springs had the same values $c_3 = c_2$. In addition, the dissipation elements b_i were considered, which were connected in parallel with the main spring c_1 and the compensation springs c_2 and c_3. Based on the presented schematic diagram, the mechanical characteristics were identified, and the differential equations of motion were derived.

2.1. Identification of mechanical characteristics

The cause-and-effect relationships between the displacement of the inertial element loading the flexible beam and the external load *F* were derived, neglecting the influence

of inertial and dissipative forces. The external load F that acts on the system was balanced by the three forces induced in the main spring c_1 and the compensation springs c_2 and c_3. The identification of the mechanical characteristics was carried out for the reference system, the beginning of which was at joint A.

$$F = F_1 + 2F_2 sin\varphi = c_1 q + 2c_2 \Delta L sin\varphi = c_1 q + 2c_2 (L_0 - L_1)\frac{(h-q)}{L_1}. \quad (1)$$

The relationships defining the lengths of the compensation springs in the static equilibrium position L_0 and at the time of their deformation L_1, are represented by the following relationships: $L_0 = \sqrt{a_0^2 + h^2}$, $L_1 = \sqrt{a_0^2 + (h-q)^2}$, where F_1 and F_2 are the forces denoted in Fig.1. After applying a few transformations, formula (1) is transformed to:

$$F = c_1 q + \underbrace{(c_2 + c_3)}_{c_K}(h-q)\left(\frac{\sqrt{a_0^2 + h^2}}{\sqrt{a_0^2 + (h-q)^2}} - 1\right) \quad (2)$$

where c_K denotes stiffness in compensation springs.

Considering the qualitative assessment of the impact of the parameters defining the mechanical characteristics and potential barriers, the following variable and parameter are introduced: $x = \frac{q}{a_0}$ and $\beta = \frac{h}{a_0}$. Taking them into account leads to a mechanical characteristic given in dimensionless form:

$$F(x) = a_0 c_1 x + a_0 c_K (\beta - x)\left(\frac{\sqrt{1+\beta^2}}{\sqrt{1+(\beta-x)^2}} - 1\right) \quad (3)$$

The relationship that defines the potential barrier is obtained as the result of integration (3). Its explicit representation is given by the following equation:

$$V(x) = \int F dx = \frac{1}{2} a_0 c_1 x^2 + a_0 c_K \left(1 - x\beta + \beta^2 + \frac{1}{2}x^2 - \sqrt{1+\beta^2}\sqrt{1+(\beta-x)^2}\right). \quad (4)$$

The moment when negative dynamic stiffness appears in the mathematical model is obtained by differentiing the mechanical characteristics (3):

$$\frac{dF}{dx} = a_0 c_1 - a_0 c_K \left(\frac{(\beta - x)^2 \sqrt{1+\beta^2}}{(1+(\beta-x)^2)^{\frac{3}{2}}} - \frac{\sqrt{1+\beta^2}}{\sqrt{1+(\beta-x)^2}} + 1 \right). \quad (5)$$

Exemplary bifurcation diagrams showing the distribution of zero-points of the mechanical characteristic (3) and its derivative (4) are presented in Figure 2. The zero-points of the mechanical characteristics are marked in blue, with the omission of the zero-point at the origin. The red color represents the distribution of the derivative's zeros along the mechanical characteristics. Based on the model tests, it is possible to distinguish three characteristic zones, separated by planes P_1 and P_2. Their position was determined by points A_1 and A_2, where the complex solution is being changed to a real one. The actual values of the solutions were distinguished by the zero plane, P_0.

In the first zone Z_I, limited by the range of variability of the control parameter $\beta \in [0, 0.458]$, the mechanical characteristic was represented by a monotonically increasing function with a single zero-point. In the second Z_{II} and the third Z_{III} zones, we deal with negative dynamic stiffness. The position of the planes separating individual zones depends on the μ coefficient, which defines the relationship between the stiffness coefficients of elastic elements. When $\beta = 1.07$, then the local minimum of the mechanical characteristic is equal to zero. In zone Z_{III}, the potential barrier is mapped to an asymmetric function with wells of different depths.

From an engineering point of view, the configuration of the compensation springs c_2 and c_3 defines two design solutions. When $\beta = 0$ we deal with a classical system of quasi-zero stiffness, the potential barrier of which is represented by a nearly-flat well [34–37]. However, when $h \gg a_0$, the parameter β takes large values, and then the compensation

springs c_2 and c_3 are oriented almost parallel to the mainspring c_1. In this case, the dynamics of the system can be accurately mapped by a linear model

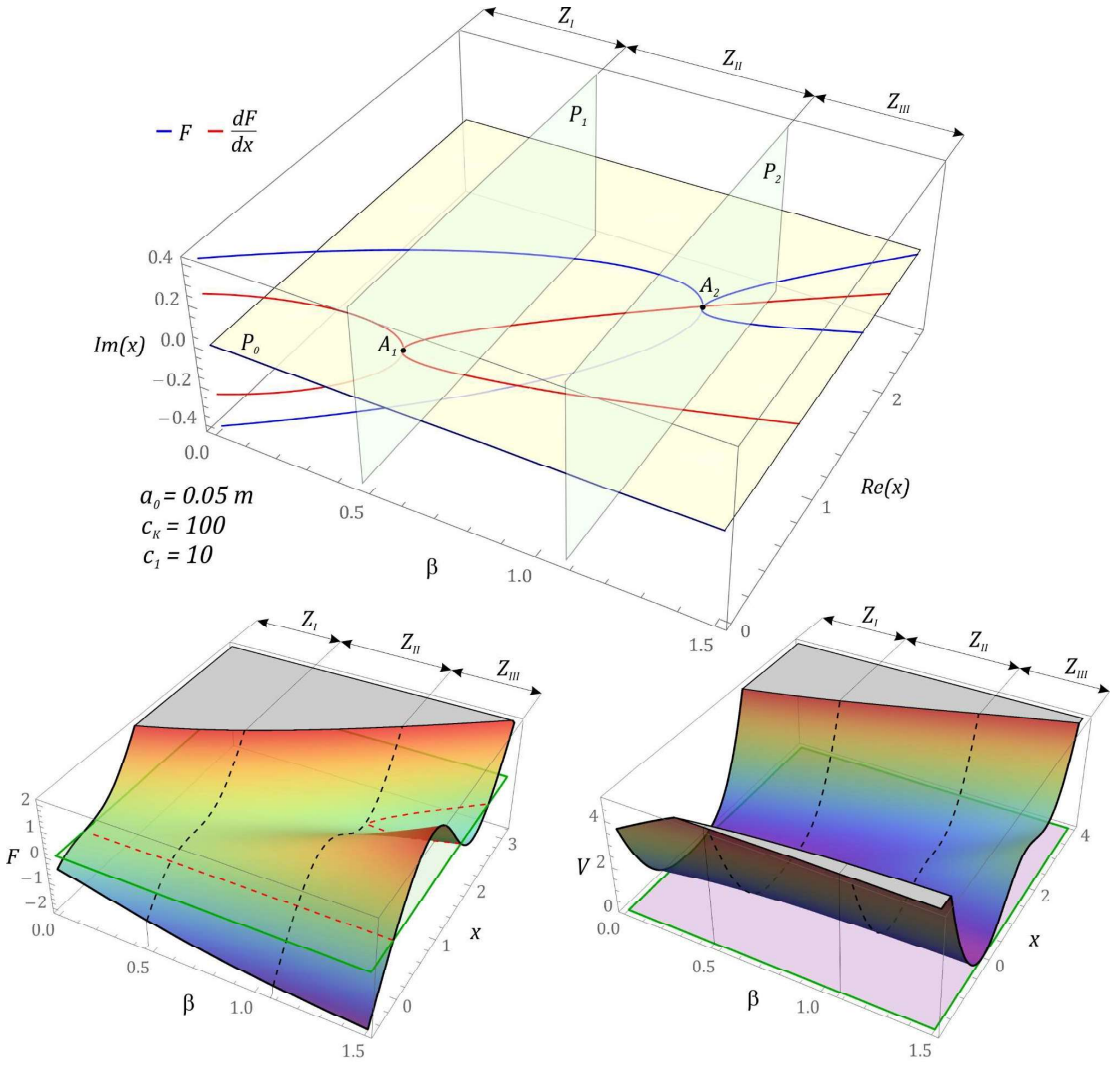

Fig. 2. Sensitivity of the parameter β to the mechanical characteristics and the potential barrier

2.2. Defining the mathematical model of the energy harvesting system

From a mathematical point of view, the energy dissipation elements b_B and b_1 form a parallel connection. For this reason, in subsequent sections, a simplification was made, which was the derivation of the equivalent dissipation element b_Z (Fig. 1a), the value of which is equal to the superposition of the dissipation properties of a flexible beam b_B and the total losses occurring in the connections of the movable compensation spring b_1. The

situation is similar to the elastic element modeling the stiffness of the c_B beam and the main spring c_1, the equivalent stiffness of which takes the values determined by the relation $c_Z = c_B + c_1$ (Fig 1a). Because of this simplification, it is necessary to increase the stiffness of the mainspring c_1 by the value c_B. Moreover, we assume that the system is influenced by harmonic excitation. Bearing in mind the adopted model and simplifying assumptions, the differential equations of motion, which also take into account the new variable $y = q - f$, take the form:

$$\begin{cases} m\frac{d^2q}{dt^2} + b_B\left(\frac{dq}{dt} - \frac{df}{dt}\right) + b_1\left(\frac{dq}{dt} - \frac{df}{dt}\right) + b_K\left(\frac{dq}{dt} - \frac{df}{dt}\right)sin\varphi + c_B(q-f) + \\ c_1(q-f) + c_K\big(h-(q-f)\big)\left(\frac{\sqrt{a_0^2+h^2}}{\sqrt{a_0^2+\big(h-(q-f)\big)^2}} - 1\right) + k_P U = 0, \\ \frac{dU}{dt} + \frac{1}{C_P R_Z}U - \frac{k_P}{C_P}\left(\frac{dq}{dt} - \frac{df}{dt}\right) = 0, \end{cases} \tag{6}$$

where:

$f = Asin(\omega_W t)$ is the kinematic excitation.

The electrical subsystem coefficients in the mathematical model (6) represent a constant k_P and piezoelectric capacity C_P. On the other hand, when using the R_Z parameter, the equivalent resistance of the piezoelectric electric circuit was mapped. The above equations can be written in the following simplified form:

$$\begin{cases} \ddot{x} + \left(\mu + \frac{(\beta - x)}{\sqrt{1+(\beta-x)^2}}\right)\delta\dot{x} + \eta x + (\beta - x)\left(\frac{\sqrt{1+\beta^2}}{\sqrt{1+(\beta-x)^2}} - 1\right) \\ +\theta U = \omega^2 psin(\omega\tau), \\ \dot{U} + \sigma U - \vartheta\dot{x} = 0, \end{cases} \tag{7}$$

where:

$$\mu = \frac{b_Z}{b_K}, \quad \eta = \frac{c_Z}{c_K}, \quad \omega_0^2 = \frac{c_K}{m}, \quad \delta = \frac{b_K}{m\omega_0}, \quad x = \frac{y}{a_0}, \quad p = \frac{A}{a_0}, \quad \omega = \frac{\omega_W}{\omega_0},$$
$$\theta = \frac{k_P}{ma_0\omega_0^2}, \quad \vartheta = \frac{k_P a_0}{C_P}, \quad \sigma = \frac{1}{\omega_0 C_P R_Z}, \quad \beta = \frac{h}{a_0}, \quad \tau = \omega_0 t.$$

Based on these formulated mathematical models of an energy harvesting system with tunnel mechanical characteristics, model tests will be presented in the following sections.

3. The results of model tests

Numerical experiments to map the dynamics of the tested energy harvesting system were carried out with reference to the numerical data summarized in Table 1.

Table 1. Geometric and physical parameters of the model

Name	Symbol	Value
Inertial element (mass) loading the beam	m	$0.03\ kg$
Energy losses in a mechanical system	δ	$0.138\ Nsm^{-1}$
Stiffness of the main springs	c_1	$10\ Nm^{-1}$
Stiffness of the compensation springs	c_2, c_3	$50\ Nm^{-1}$
Damping of the main spring	b_1	$0.024\ Nsm^{-1}$
Damping of the springs	b_2, b_3	$0.012\ Nsm^{-1}$
Stiffness of the beam	c_b	$15\ Nm^{-1}$
Damping of the beam	b_b	$0.012\ Nsm^{-1}$
Stiffness ratio of elastic elements	μ	0.1
Length of the compensation springs at the equilibrium position	a_0	$0.03\ m$
Total resistance	R_Z	$2.41 \cdot 10^6\ \Omega$
Equivalent capacity of the piezoelectric converter	C_P	$21.67\ nF$
Electromechanical constant of piezoelectric converter	k_P	$12.24 \cdot 10^{-5}\ N/V$

Based on the numerical data characterizing the mathematical model, numerical experiments were carried out to show the impact of the dimensionless frequency ω, the excitation amplitude p, and β parameter on the location of the zones of chaotic solutions. For

this purpose, a numerical algorithm was used, on the basis of which the value of the largest Lyapunov λ exponent could be determined [38,39]. In our case, the results of the model tests were visualized in the form of multi-colored maps, which were plotted at a resolution of 600 × 600 points of the variability range of the control parameters ω and p. Additionally, the characteristic points of the multi-colored maps of the distribution of the largest Lyapunov exponent were related to the diagrams of the RMS voltage induced on the piezoelectric electrodes. The effective value of the induced voltage U_{RMS} on the piezoelectric electrodes was adopted as an indicator representing the energy harvesting efficiency. Diagrams of the energy harvesting efficiency were drawn with the assumption that the system was in a steady-state after 600 periods of excitation. The effective value was estimated based on the time window with a width equal to 50 periods of excitation. Exemplary results of computer simulations are shown in the graphs in Fig. 3.

The areas of chaotic solutions are distinguished by yellow and orange ($\lambda > 0$). The periodic responses were distinguished by shades of blue ($\lambda < 0$), and green near $\lambda \approx 0$, where were so-called bifurcation points. The multi-colored maps of the distribution of the largest Lyapunov exponent indicated that upon increasing β, the zones of complex solutions expanded. Nevertheless, with regard to large values of β ($\beta \gg 2$), the areas of complex solutions migrated towards higher values of the dimensionless exciattion amplitude p, and the dynamics of the system were mapped through a corresponding linear mathematical model. This behavior of the system occurred because the compensation springs c_2 and c_3 were then oriented almost parallel to the main spring c_1 (Fig. 1).

Regardless of the value of the parameter β, the amplitude of vibrations influencing the tested system had a significant impact on the efficiency of the harvesting energy, and the highest voltages were induced on the piezoelectric electrodes close to $\omega = 1$. Near $\omega = 1$, increasing p significantly affected the ability to harvest energy, but at higher ω values, it

was not so significant. As there were zones in which, after exceeding the appropriate amplitude of external vibrations *p*, its further increase did not affect the value of the voltage induced on the piezoelectric electrodes. For example, we deal with such cases in the bands $\omega \in [Z_2, Y_3]$ (Fig. 3a), $\omega \in [Z_4, Y_3]$ (Fig. 3b). This situation to a lesser extent took place at higher values of the parameter β $\omega \in [Y_4, Y_5]$ (Fig. 3c), $\omega \in [Y_4, Y_5]$ (Fig. 3d).

Based on a direct comparison of the diagrams of RMS voltage induced on the piezoelectric electrodes with the maps of the distribution of the largest Lyapunov exponent, it can be concluded that at the boundaries of chaotic and periodic solutions, there was an increase or decrease in the harvesting energy efficiency (Fig. 3). It is worth noting that in the bounded areas of the system response change, there were "faults" observed in the diagrams of RMS voltage values, which indicate a reduction or increase in the energy harvesting capacity. At the same time, based on the presented examples, a reduction in the harvesting energy efficiency was observed when changing the periodic solution into a chaotic one.

The presented examples suggest that to effectively generate energy through a system with tunnel mechanical characteristics, in a wide range of variability, ω, the areas of periodic and chaotic solutions should alternate. This proves the sequence of bifurcations and the variability of solutions when changing ω. The width of the bands of chaotic solutions should be narrow enough to minimize the voltage drops induced on the piezoelectric electrodes.

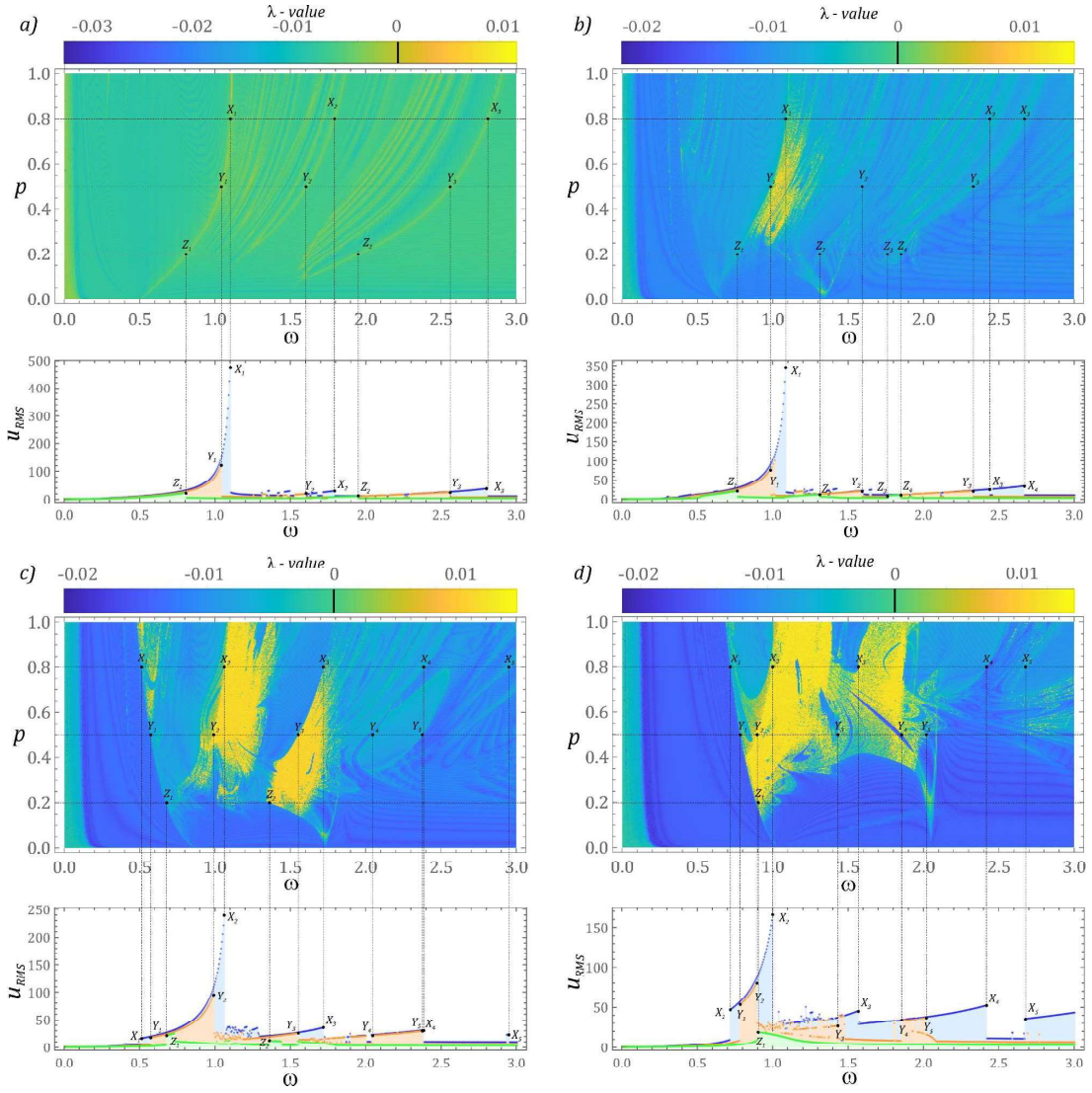

Fig. 3. Influence of β on the distribution of the largest Lyapunov exponent: a) β = *0*, b) β = *0.5*, c) β = *1*, d) β = *2*

Then, computer simulations were carried out to determine the optimal configuration of the tunnel energy harvesting system. As in the numerical experiments presented, zero initial conditions were assumed. The results of preliminary model studies indicated that the cause-and-effect relationship, given by parameter β, that determines the configuration of the compensation springs c_2 and c_3 relative to the main spring c_1, has a significant impact on the bands in which harvesting energy is most effective. In the next stage of the research, the results of optimization with regard to β will be presented.

3.1. Optimal configuration of the elastic elements

From a theoretical point of view, the optimization criteria can be formulated in different manner. From the point of view of the model tests carried out, we are interested in sustainable generating energy in a wide range of excitation frequencies. Therefore, the A_{RMS} indicator (Fig. 4), representing the optimization criterion, was defined as the area under the diagram of RMS values of the voltage induced on the piezoelectric electrodes. Systems with non-linear dynamics, similarly to systems based on linear oscillators, also require tuning, but in the case of linear oscillators this comes down to tuning to the excitation frequency. In the case of a non-linear system, the TEEH is tuned in accordance to the excitation amplitude. In the numerical experiments, the influence of β was investigated over a relatively wide variability range. In practical solutions, the β variability range significantly depends on the design of the energy harvesting system with tunnel mechanical characteristics. Therefore, when identifying the optimal configuration of the compensation springs with respect to the main spring, the range of variation was limited to $\beta \leq 3$. For practical applications the β value can be adjusted in two ways – by change of the h value – its increasing is not recommended because it leads to an increase in the dimensions of the system. The second way is to change the distance a_0. But when $a_0 \approx 0$ we are dealing with a linear oscillator. In the case when $\beta=0$, as a result of which the compensation springs assume a horizontal configuration in relation to the frame, we are dealing with a quasi-zero stiffness energy harvesting system.

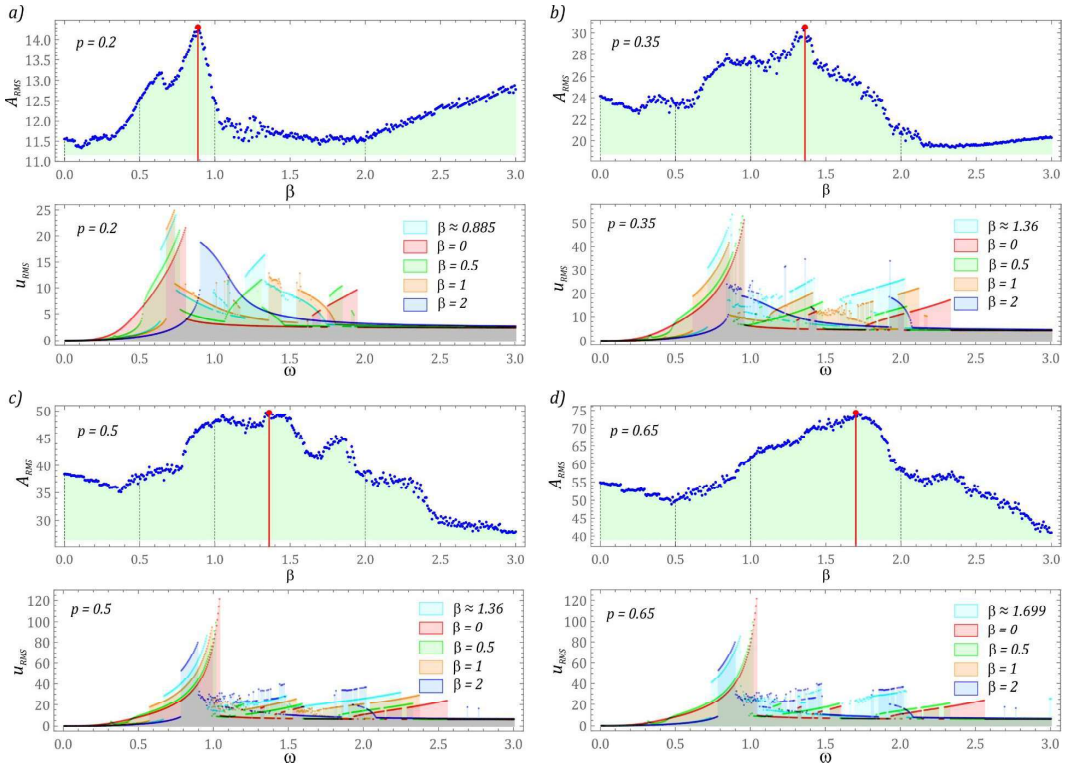

Fig. 4. Optimization of the configuration of the elastic elements. The colors indicate the results of various β parameters.

Regarding the selected values of the dimensionless amplitude of vibrations affecting the energy harvesting system with tunnel mechanical characteristics, the diagrams of the A_{RMS} surface areas are presented in Fig.4. The largest are highlighted in red. In the range of large values $\omega > 2.5$, the configuration of the compensation springs relative to the main one did not affect the induced voltage. This situation occurred because the U_{RMS} effective voltage diagrams, plotted for different values of β, at the end of the analyzed range of the dimensionless frequency $\omega = 3$, asymptotically approached the determined value. Regarding the presented computer simulation results, the mean RMS voltages were $U_{RMS} \approx 2.51 \pm 0.09$ (Fig. 4a), $U_{RMS} \approx 4.42 \pm 0.16$ (Fig. 4b), $U_{RMS} \approx 6.3 \pm 0.23$ (Fig. 4c), and $U_{RMS} \approx 8.14 \pm 0.27$ (Fig. 4d). It is worth noting that the largest surface area was not the same as the largest possible recorded voltage value. Based on the results of model tests presented in the case

and illustrated by in Fig. 4d, the voltage recorded on the electrodes reached the highest values for the optimal value of β=1.699.

3.2. Identification of coexisting solutions

The results of the research presented in the preceding subsection reflect some special cases of the dynamics of the energy harvesting system, determined by zero initial conditions. Such a description of dynamics is valid when the energy harvesting system is excited from the equilibrium position. Bearing in mind the impact on the nature of the solution, it is necessary to know coexisting solutions—a characteristic property of nonlinear systems. For this reason, numerical experiments were conducted to identify them. This problem comes down to a study of orbits, the origins of which are in different parts of the phase plane. Considering the research problem formulated in this way, it is possible to carry out numerical calculations, the results of which are presented in the form of a diagram of solutions (DS, black points). This diagram consists of two overlapping charts, a diagram of periodic solutions (DPS) and a diagram of solutions number (DNS, bar graph in green), both of which are synchronized with the frequency footer [25]. In such an approach, information about the ability of obtaining electrical energy was neglected. However, information was available on the number of coexisting solutions and their periodicity. In general, this procedure relies upon examining Poincaré sections plotted for various initial conditions.

To identify the energy harvesting efficiency, the effective voltage recorded at the receiver was calculated. In this case, the model research also comes down to examining the initial conditions. The simulations result is a diagram with branches representing the recordable voltage of the harvester. The obtained *DS* and the diagrams of U_{RMS} values are

plotted in a simplified manner because their accuracy is a compromise between calculation precision and computer simulation time. For this reason, to refine the results, additional computer simulations are most often performed with greater accuracy. On their basis, it is possible to precisely assign the periodicity of the solution to individual branches of the effective voltage diagram. It is worth mentioning that each of the diagrams is plotted for randomly-selected initial conditions. Regarding simple structures depicting the diagrams, additional numerical experimentation is not necessary. However, to facilitate the interpretation of the obtained results, each branch of the U_{RMS} diagram (points in red) was assigned a solution periodicity. The following convention was adopted when describing the branches: the large number preceding the letter T indicates the periodicity of the solution, while the digit in the right subscript is the number of solutions for a given periodicity and *Ch* means chaos (Fig.5).

In the following diagrams in Figure 5 coexisting solutions are provided. On their basis, it is possible to determine the ranges of the variability of the dimensionless frequency ω that provides the most effective energy harvesting. Here, the coexisting solutions and diagrams of RMS voltage induced on piezoelectric electrodes were identified in the phase space limited by the values $x_i \in$ [-2, 2] and $\dot{x}_i \in$ [-2, 2]. The single points in the DS diagrams represent unstable periodic solutions with high periodicity, which over time become attracted to permanent periodic solutions with relatively low periodicity. To a lesser extent, this can be interpreted as artifacts related to numerical errors. Most of these points can be reduced by increasing the computer simulation time, however, the latter is related to a drastic extension of numerical calculations. Such solutions are most often found in complex diagrams with relatively narrow bands of chaotic responses. Such a situation may also arise when an increase in the dimensionless frequency ω rapidly influences changes in the response characteristics of the system (β = 1.36, p = 0.35).

When the configuration of the mainspring with respect to the compensation springs takes the value $\beta = 0$, the potential characteristic is represented by a quasi-flat well. It is worth noting that regardless of the value of the dimensionless vibration amplitude p, there are clearly-distinguished zones in which multiple solutions occur. These zones coincide with the branches of the effective voltage diagram induced on the piezoelectric electrodes. Periodic solutions with a $1T$ periodicity dominate the entire studied range of ω. Such responses dominate the range of low and very high values of ω. The limiting values are determined by the characteristic representing the shape of the potential barrier and the level of vibrations affecting the energy harvesting system.

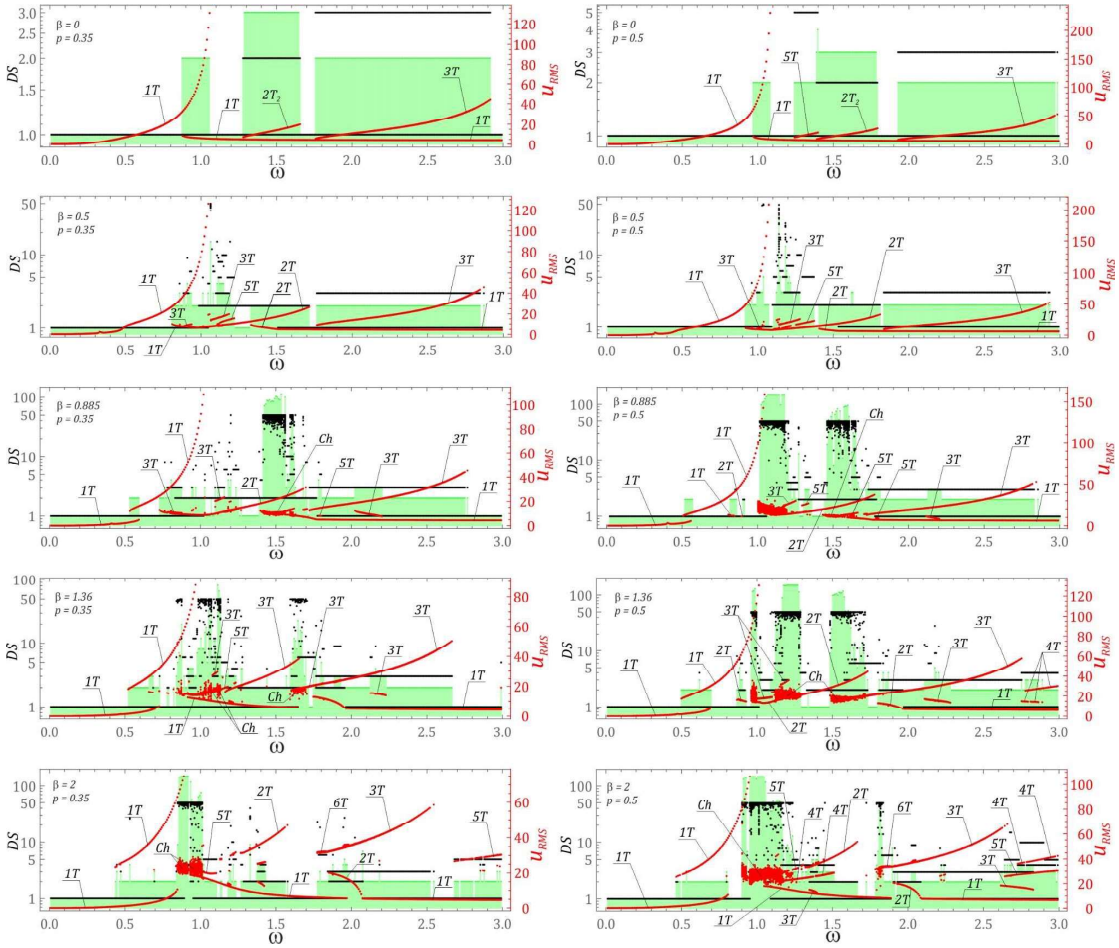

Fig. 5. Diagrams of coexisting solutions and the effective voltage induced on piezoelectric electrodes. DS diagrams represent the periodicity and number of stable periodic and chaotic solutions

Double-symmetrical solutions were observed for the case ($\beta = 0$, $p = 0.35$) in the limited band $\omega \in [1.27, 1.65]$. $3T$ periodic solutions dominated the widest bands of a coexisting solutions DS. In the examples provided, when $\beta = 0$, the DS has a simple structure, which becomes more and more complex upon increasing β. The complexity is determined by the emergence of areas where complex solutions occur. The excitation of chaotic solutions is also caused by an increase in the p-value of the dimensionless amplitude of vibrations affecting the tested energy harvesting system (comparison $\beta = 0.5$, $p = 0.2$ and $\beta = 0.5$, $p = 0.35$). This system behavior directly results from analyzing the multi-colored maps of the distribution of the largest Lyapunov exponent λ (Fig. 3).

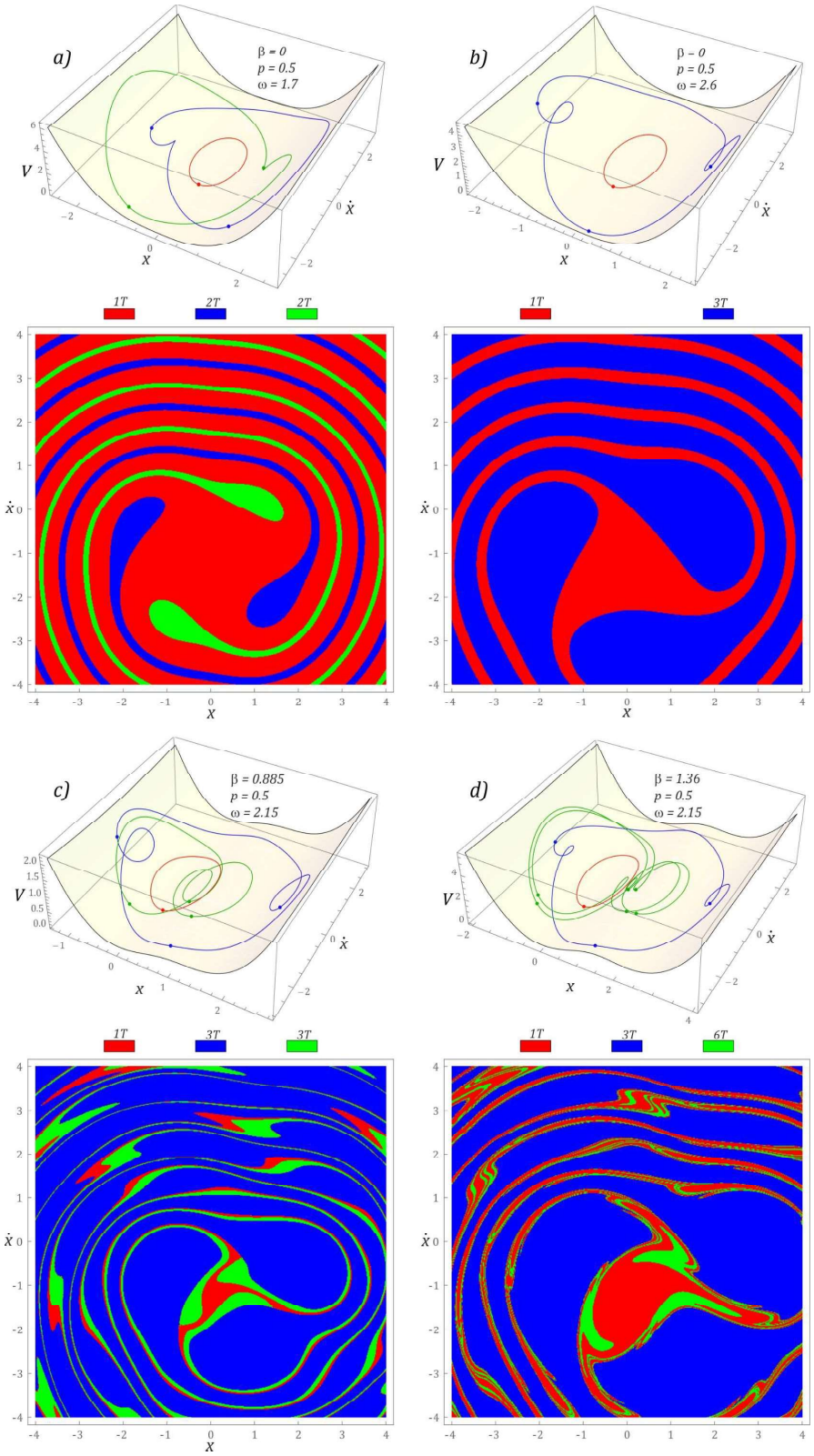

Fig. 6. Images of coexisting periodic solutions including the basins of attraction and phase portraits (with the potential energy states)

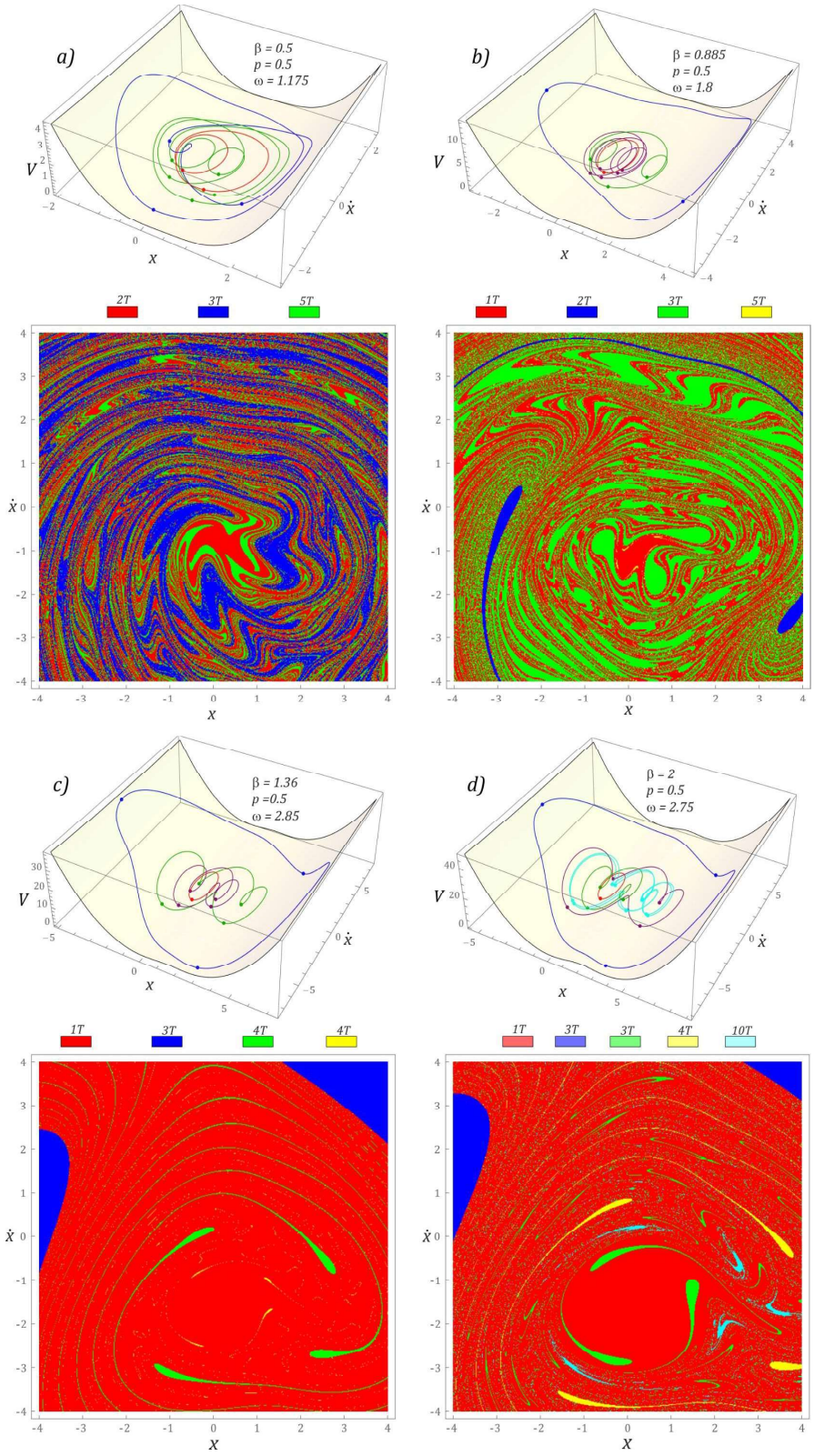

Fig. 7. Images of coexisting periodic solutions including the basins of attraction and phase portraits (with the potential energy states)

Near a harmonic component ω = 1, a system with a tunnel characteristic shows the highest values of the effective voltage induced on the piezoelectric electrodes when β = 0 and at low *p* values. An increase in the level of vibrations affecting the energy harvesting system shifting its efficiency towards higher values of ω. On the other hand, modifying the shape of the potential barrier by increasing β causes the efficicency to shift towards low values of ω.

The convention is as follows when plotting the basins of attraction: the color of the basin of attraction corresponds directly to the color of the orbit. The corresponding orbits are plotted in purple only for the basins of attraction highlighted in yellow. This was done because depicting the phase trajectory in yellow would be unreadable against the background of the three-dimensional potential barrier. Table 2 summarizes the quantitative indicators characterizing the effective voltages induced on the piezoelectric electrodes and the areas of basins of attraction of coexisting solutions. The size of the basins of attraction was estimated by counting the initial conditions leading to the individual solutions. On this basis, we can also determine the probability of a given response.

Table 2. Numerical indicators characterizing permanent solutions with the voltage output and corresponding solutions

Parameter Values			*Solution – I*	*Solution – II*	*Solution – III*	*Solution – IV*	*Solution – V*
β	*p*	ω					
0	*0.5*	*1.7*	$u_{RMS} = 6.6V$ *A = 73%*	$u_{RMS} = 22.21V$ *A = 15%*	$u_{RMS} = 22.31V$ *A = 12%*		
0	*0.5*	*2.6*	$u_{RMS} = 6.15V$ *A = 31%*	$u_{RMS} = 25.57V$ *A = 69%*			
0.5	*0.5*	*1.175*	$u_{RMS} = 9.86V$ *A = 42%*	$u_{RMS} = 18.75V$ *A = 32%*	$u_{RMS} = 12.07V$ *A = 26%*		

0.885	*0.5*	*1.8*	$u_{RMS} = 6.97V$ $A = 48\%$	$u_{RMS} = 39.85V$ $A = 2\%$	$u_{RMS} = 15.16V$ $A = 47\%$	$u_{RMS} = 8.78V$ $A = 3\%$	
0.885	*0.5*	*2.15*	$u_{RMS} = 6.62V$ $A = 8\%$	$u_{RMS} = 21.88V$ $A = 78\%$	$u_{RMS} = 9.91V$ $A = 14\%$		
1.36	*0.5*	*2.15*	$u_{RMS} = 7.1V$ $A = 21\%$	$u_{RMS} = 29.37V$ $A = 69\%$	$u_{RMS} = 16.52V$ $A = 9\%$		
1.36	*0.5*	*2.85*	$u_{RMS} = 6.51V$ $A = 90\%$	$u_{RMS} = 68.63V$ $A = 6\%$	$u_{RMS} = 27.56V$ $A = 3\%$	$u_{RMS} = 14.47V$ $A = 1\%$	
2	*0.5*	*2.75*	$u_{RMS} = 6.76V$ $A = 84\%$	$u_{RMS} = 77.37V$ $A = 4\%$	$u_{RMS} = 16.56V$ $A = 7\%$	$u_{RMS} = 36.91V$ $A = 2\%$	$u_{RMS} = 27.57V$ $A = 3\%$

The graphs in Figure 6 and Figure 7 show selected examples of permanent periodic solutions. Their visualization was limited to the case when the tested energy harvesting system was influenced by mechanical vibrations given a dimensionless amplitude $p = 0.5$. This was done because, regardless of the excitation level, the permanent solutions showed similar topologies. No direct comparison of the structures of the basins of attraction for the same values of the dimensionless excitation frequency was carried out because the plotted diagrams of coexisting solutions (Fig. 5) clearly indicate a shift towards lower values of ω. The primary purpose of the plotted basins of attraction was to relate them directly to the band distribution in the impulse excitation diagrams.

The solutions with the worst energy efficiency $u_{RMS} < 10$ V, have 1T-periodicity and are located in the potential barrier well. Homogeneous, distinct boundaries of basins of attraction occur in the range of low values of the state variables. In the examples under consideration, such a separation of the basins of attraction occurs only in three cases (Fig. 6a, b, and c). In the remaining examples, the boundaries of the basins of attraction are essentially blurred (Fig. 7). For some basins of attraction (mapped in blue and green) there are

homogeneous clear boundaries. In addition, it is worth noting that as we move away from the "center of rotation" of the drawn map, we can observe increasingly blurred boundaries. Nevertheless, clear homogeneous boundaries are observed for some coexisting solutions. Such basins of attraction edges occur near their center of gravity. Here, by the center of gravity, we mean the point relative to which the basins of attraction are hypothetically "pivoting". In the example (Fig. 6a), the sizes of the basins of attraction of $2T$-periodic solutions slightly differ, the difference being directly related to the shift of the center of gravity towards negative values of the phase plane velocity. It is also worth noting that we deal with such shifts related to each of the presented basin of attraction.

4. The influence of impulse disturbance on the ability to harvest energy

Dynamic vibrational excitations caused by the operation of the machine, which affect a person and devices, are subject to disturbances. When such a disturbance of the excitation signal appears in non-linear systems, the solution may change. This change can have a positive impact on the efficiency of energy harvesting as well as a negative impact. In this section, numerical experiments were carried out to assess the impact of the F_S excitation impulse on the nature of the solution and the energy harvesting efficiency. From a theoretical point of view, such an impulse may disturb the vibration signal or directly act, via an external electromechanical subsystem, on the inertial element m loading the free end of the flexible cantilever beam (Fig. 1). Here, we indicate that the research results do not consider the dynamics of such a subsystem, and we treat the disturbing impulse itself as ideal.

During computer simulations, it was assumed that at the initial moment, the flexible cantilever beam I was in a position of static equilibrium ($x(0) = 0, \dot{x}(0) = 0$). Moreover, we *a priori* assumed that the disturbing impulse was initiated when the energy harvesting

system was in the steady-motion state. In other words, from the moment $\tau = 0$, the kinematic excitation $f = Asin(\omega_W t)$ from which the energy is harvested affect the structure under study. In the steady-state response when we deal with a stable attracting solution, the excitation impulse F_S is initiated. The appearance of an additional dynamic interaction causes the operating point to be precipitated from a stable orbit (corresponding to zero-initial conditions), which was mapped in red (Fig. 8). After the work point is knocked out of the stable orbit, the trajectory highlighted in gray, over time, tends to one of the permanent periodic solutions. Red markers represent the Poincaré points of the solution corresponding to zero-initial conditions, blue markers represent the Poincaré points of the target orbit. The moments at which the impulse initiation occurs are marked with black markers and white markers show its withdrawal. The black curve represents the phase trajectory of the system response during the F_S impulse.

Bearing in mind the determination of the optimal value of the excitation impulse initiation time $\tau = 0$, a numerical procedure was developed plotting the so-called impulse excitation diagram (IED). In general, the procedure involves the identification of Poincaré points of the phase trajectory disturbed by the F_S impulse. The identified Poincaré points are compared with the Poincaré points of individual coexisting solutions. The graphs in Fig. 8 show the results of computer simulations, which also show the influence of the characteristics of the excitation impulse on its structure. We assume that the ratio of the impulse height to its width is $F_S/\tau_1 = 3$ or $1/3$. The gray rectangles represent the moments of initiation of the disturbing impulse. The area of the rectangle is the product of the amplitude and the time of the impulse. At the present stage of modeling, the amplitude of the disturbing impulse was assumed to be close to the maximum acceleration of mechanical vibrations affecting the energy harvesting system.

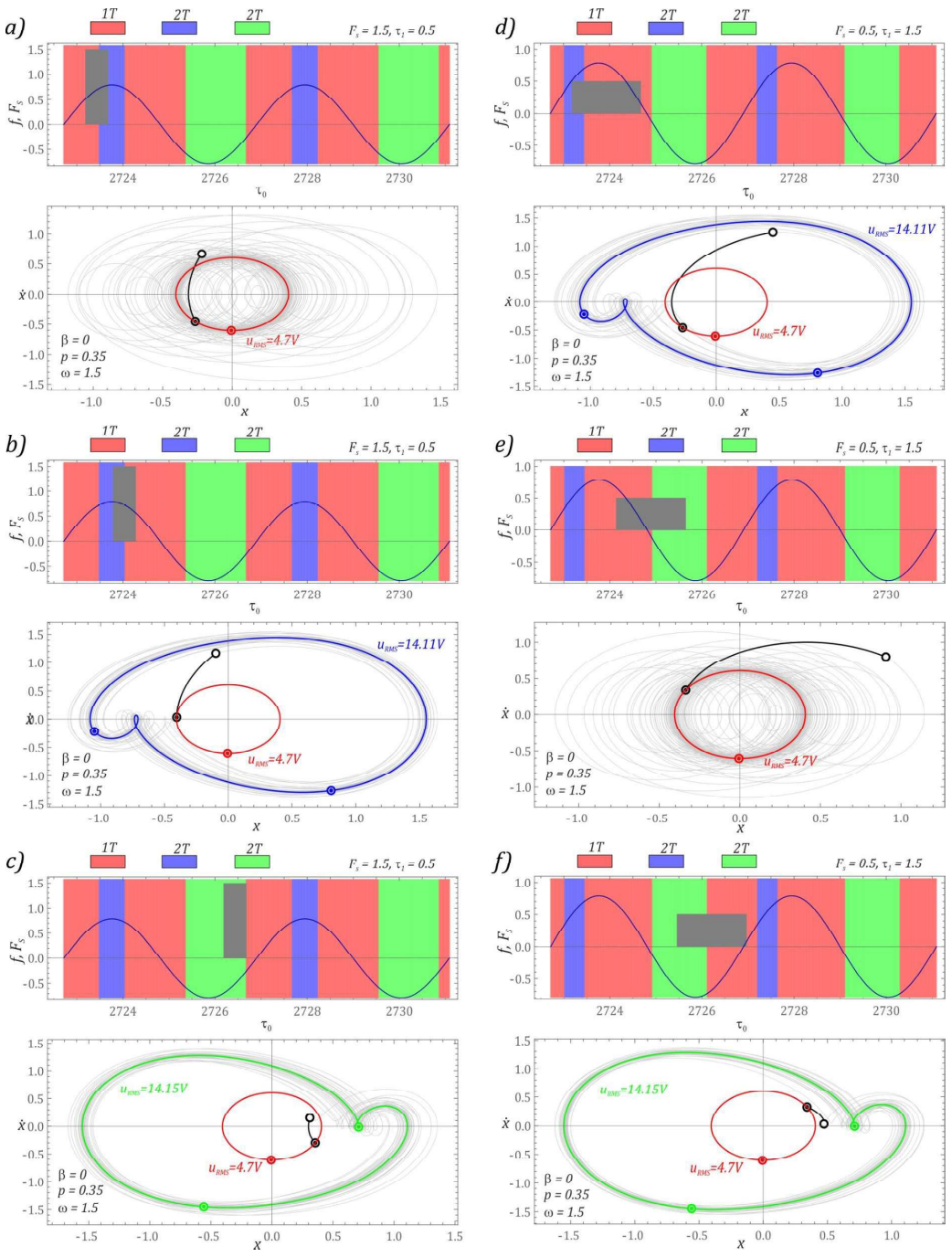

Fig. 8. Influence of the impulse orientation on the structure of the IED. The colors represent different solutions and orbits. Gray is the color of the impulse

IEDs (Fig. 8) were plotted with reference to the time windows, with width equal to twice the periodicity of the solution with the lowest voltage induced on the piezoelectric electrodes. This convention was adopted in relation to the impulse excitation diagrams,

which are presented. The navy-blue color in the diagram represents the signal of mechanical vibrations that affect the tested energy harvesting system. The presented results show the correctness of the adopted model assumptions. The colors of the IED diagram bands directly correlate with the colors of the orbits of the coexisting periodic solutions. The visual analysis of the band distribution in the diagrams appears to be similar. Nevertheless, the direct reference of the vertical-horizontal plots displays a shift relative to the axis τ_0, and the variable width of the bands corresponds to individual solutions. The sequence of the individual bands does not change. The surface area under the impulse characteristic is the same for both vertical and horizontal orientations. The choice of the impulse orientation largely depends on the design of the external system responsible for its initiation at the right moment. For subsystems with fast response times, vertical orientation is recommended (Fig. 8a-c); however, for systems with a relatively long reaction time, a horizontal orientation is recommended (Fig. 8d-f). Regardless of the orientation of the impulse initiating the disturbance of the permanent solution, the individual parts of the diagram form a regular, cyclically-repeating structure.

In the example, there are three periodic solutions: one 1T-periodic and two 2T-periodic solutions. In the plots (Fig. 8a and e), there are events where the disturbing impulse is initiated at the wrong time τ_0. An incorrect moment of impulse initiation causes the operating point, which has been precipitated from its stable orbit, to return to the starting orbit after the transient processes are extinguished. In other words, the exit and target trajectories coincide. The correctly selected initiation time of the disturbing impulse, which changes the solution, is shown in the cases in the remaining graphs (Fig. 8). All other examples correspond to the optimal (in the given excitation conditions) harvesting energy because the orbits of the coexisting solutions are characterized by comparable voltages induced on the piezoelectric electrodes.

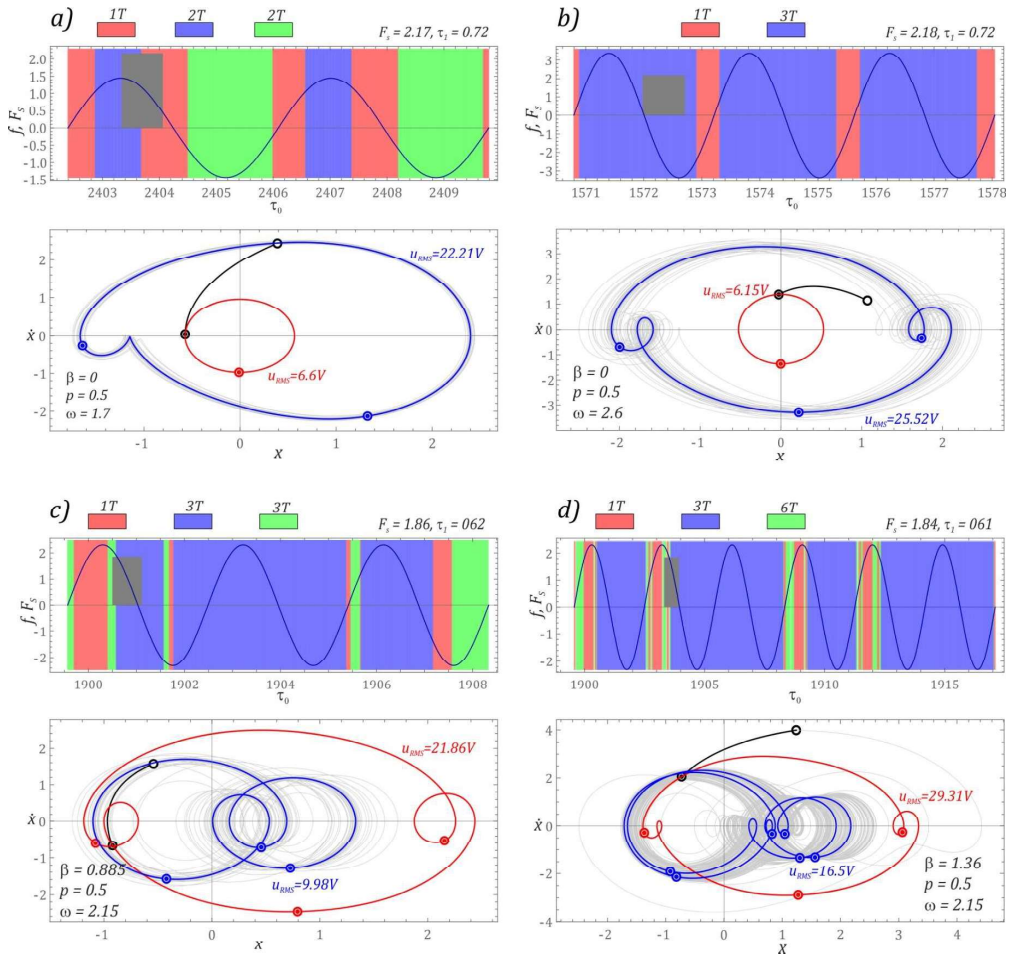

Fig. 9. Impulse excitation diagrams for the coexisting solutions. The colors represent different solutions and orbits. Gray is the color of the impulse

In addition, graphical images of impulse excitation diagrams are shown, which are plotted against the examples in the graphs (Figs. 6 and 7). The exit orbit (corresponding to zero initial conditions) and target orbit are depicted, which are characterized by the best harvesting energy efficiency from a mechanically vibrating object. In a situation where zero-initial conditions lead to the solution with the best energy efficiency, the target orbit was chosen from any of the coexisting solutions. We note that the exit orbits were drawn in red, while the target orbits were mapped in blue.

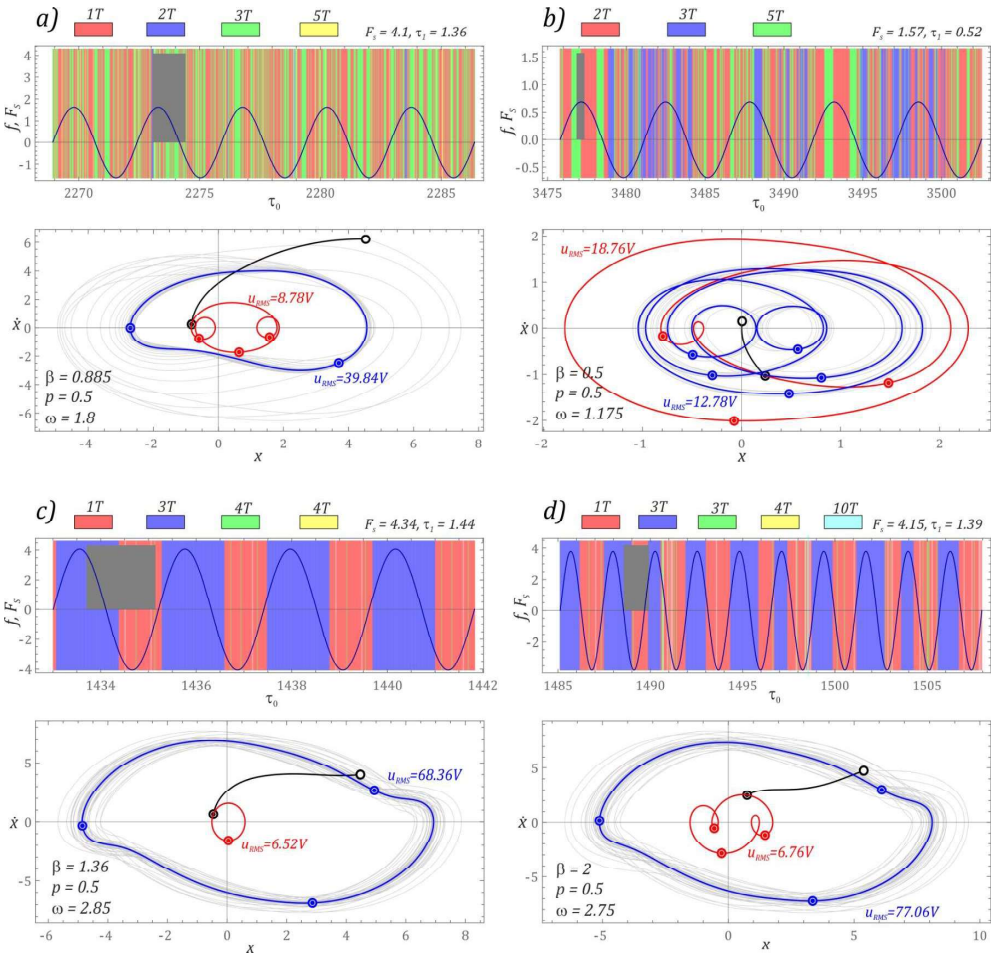

Fig. 10. Impulse excitation diagrams for the coexisting solutions. The colors represent different solutions and orbits. Gray is the color of the impulse

During the computer simulations, it was assumed that an impulse disturbed the signal of mechanical vibrations influencing the energy harvesting system. In the examples (Figs. 10a and 10b), the amplitude of the impulse is much greater than the amplitude of the vibrations acting on the energy harvesting system. Such large values were adopted because, for weaker impulses, not all solutions were achieved. Regarding the considered threecases, the zero initial conditions led to a solution inducing the highest voltages on the piezoelectric electrodes (Fig. 10b, Fig. 9c, and Fig. 9d). These results suggest that any event occurring in the environment of the device from which energy is obtained may significantly limit its harvesting efficiency. It is worth noting that the band structure of the IED is directly correlated with the basins of attraction. In other words, if the basins of

attraction of coexisting solutions are separated by clear, uniform boundaries, then the bands of the individual diagram solutions are characterized by a regular distribution of colors along the axis τ_0, as in the examples: (Fig. 9b). In the case of the fractal boundaries of the basins of attraction, the IED bands are represented by an irregular arrangement of colors (Fig. 9c-d). There is another correlation between the basins of attraction and the impulse excitation diagram. Solutions whose basins of attraction have small sets of initial conditions have narrow bands in the diagrams in which an impulse can be initiated (Fig. 10 a-b).

If the phase trajectory (black) drawn during the impulse duration ends near the targeted orbit, then the excited transient processes disappear relatively quickly. Such a situation takes place in the case depicted in the diagram (Fig. 9a). In the examples in Fig. 9c, Fig. 10c, and Fig. 10d, the endpoint of the trajectory in the duration of the impulse also terminates near the targeted orbits. Nevertheless, the time for the disappearance of the transient processes is much longer than in case shown in Fig 9a.

5. Conclusions

This paper presented model studies the tunnel mechanical characteristics energy harvesting system. Furthermore, the influence of the configuration of the compensation springs in relation to the main spring on the energy generation efficiency was investigated. In this paper we limited research to relatively small vibration amplitudes. All the results of computer simulations included in the work were carried out for the data contained in Table 1. These parameters were constant and did not change. The only parameter that was modified was the h dimension, on the basis of which the β value was determined. If β and a_0 are known, it is possible to calculate what h is - that is, what is the configuration. In each graph showing the results of numerical experiments, the β value from

the simulation is given. In the case of environmental conditions modeling the external impact of mechanical vibrations on the energy harvesting system, the parameters of the dimensionless excitation amplitude p and ω frequency were also given. In summary, based on the model tests performed, it is possible to formulate the following conclusions.

- To effectively harvest energy from vibrating mechanical systems, the operating point of the system should be located outside of the zones of chaotic solutions. This is directly related to the fact that when the dimensionless frequency of excitation ω passes through the "fault", a sharp drop in the voltage induced on the piezoelectric electrodes was observed.
- The direct presentation of a diagram of coexisting solutions and the effective values of the voltage induced on the piezoelectric electrodes, along with the identification of periodicity of individual branches, provides a complete picture of the dynamics of the energy harvesting system over a wide range of variability of the dimensionless excitation frequency ω.
- The configuration of compensation springs of the TEEH system should be carried out each time when changing the level of external mechanical vibrations affecting the system. This will effectively harvest energy over a wide range of ω. At the same time, such a procedure is advisable in relation to vibration signals, which are affected by additional disturbances.
- There was a correlation between the basins of attraction and the impulse excitation diagram. In other words, if the boundaries separating the basins of attraction form a fractal structure, then in impulse excitation diagrams, an irregular distribution of the band assigned to particular solutions is observed.

- It is recommended that when designing a nonlinear energy harvesting system, the design should always include a subsystem through which it will be possible to intentionaly influence the solution to achieve the best energy harvesting efficiency. Regarding the cases in Figure 10c and Figure 10d, the device efficiency has improved tenfold.

The computer simulation results indicate that modifying the energy harvesting system design with an impulse excitation subsystem can significantly improve the amount of energy harvested from vibrating mechanical devices. Moreover, the design of such a system should consider the possibility of regulating the configuration of the compensation springs.

Declaration of Competing Interest

The authors declare that they have no known competing financial interests or personal relationships that could have appeared to influence the work reported in this paper.

Acknowledgement

This research was funded by National Science Centre, Poland under the project SHENG-2, No. 2021/40/Q/ST8/00362.

Bibliography

[1] Wang J, Geng L, Ding L, Zhu H, Yurchenko D. The state-of-the-art review on energy harvesting from flow-induced vibrations. Appl Energy 2020;267:114902. doi:10.1016/J.APENERGY.2020.114902.

[2] Ahmad I, Hee LM, Abdelrhman AM, Imam SA, Leong MS. Scopes, challenges and

approaches of energy harvesting for wireless sensor nodes in machine condition monitoring systems: A review. Measurement 2021;183:109856. doi:10.1016/J.MEASUREMENT.2021.109856.

[3] Erturk A, Inman DJ. Piezoelectric Energy Harvesting. Piezoelectric Energy Harvest 2011. doi:10.1002/9781119991151.

[4] Litak G, Friswell MI, Kitio Kwuimy CA, Adhikari S, Borowiec M. Energy harvesting by two magnetopiezoelastic oscillators with mistuning. Theor Appl Mech Lett 2012;2:043009. doi:10.1063/2.1204309.

[5] Kim P, Son D, Seok J. Triple-well potential with a uniform depth: Advantageous aspects in designing a multi-stable energy harvester. Appl Phys Lett 2016;108:243902. doi:10.1063/1.4954169.

[6] Mitcheson PD, Yeatman EM, Rao GK, Holmes AS, Green TC. Energy harvesting from human and machine motion for wireless electronic devices. Proc IEEE 2008;96:1457–86. doi:10.1109/JPROC.2008.927494.

[7] Wang J, Liao W-H, Cao J. Power enhancement of a monostable energy harvester by orbit jumps: J Intell Mater Syst Struct 2021;32:2601–14. doi:10.1177/1045389X211006912.

[8] Tan T, Zuo L, Yan Z. Environment coupled piezoelectric galloping wind energy harvesting. Sensors Actuators A Phys 2021;323:112641. doi:10.1016/J.SNA.2021.112641.

[9] Zhou Z, Qin W, Zhu P, Du W. Harvesting more energy from variable-speed wind by a multi-stable configuration with vortex-induced vibration and galloping. Energy 2021;237:121551. doi:10.1016/J.ENERGY.2021.121551.

[10] Wang J, Yurchenko D, Hu G, Zhao L, Tang L, Yang Y. Perspectives in flow-induced vibration energy harvesting. Appl Phys Lett 2021;119:100502.

doi:10.1063/5.0063488.

[11] Mehdipour I, Madaro F, Rizzi F, De Vittorio M. Comprehensive experimental study on bluff body shapes for vortex-induced vibration piezoelectric energy harvesting mechanisms. Energy Convers Manag X 2022;13:100174. doi:10.1016/J.ECMX.2021.100174.

[12] Xu M, Wang B, Li X, Zhou S, Yurchenko D. Dynamic response mechanism of the galloping energy harvester under fluctuating wind conditions. Mech Syst Signal Process 2022;166:108410. doi:10.1016/J.YMSSP.2021.108410.

[13] Huang D, Zhou S, Litak G. Theoretical analysis of multi-stable energy harvesters with high-order stiffness terms. Commun Nonlinear Sci Numer Simul 2019;69:270–86. doi:10.1016/j.cnsns.2018.09.025.

[14] Younesian D, Alam MR. Multi-stable mechanisms for high-efficiency and broadband ocean wave energy harvesting. Appl Energy 2017;197:292–302. doi:10.1016/j.apenergy.2017.04.019.

[15] Zhou Z, Qin W, Yang Y, Zhu P. Improving efficiency of energy harvesting by a novel penta-stable configuration. Sensors Actuators, A Phys 2017;265:297–305. doi:10.1016/j.sna.2017.08.039.

[16] Lai YC, Hsiao YC, Wu HM, Wang ZL. Waterproof Fabric-Based Multifunctional Triboelectric Nanogenerator for Universally Harvesting Energy from Raindrops, Wind, and Human Motions and as Self-Powered Sensors. Adv Sci 2019;6. doi:10.1002/advs.201801883.

[17] Wang W, Cao J, Zhang N, Lin J, Liao WH. Magnetic-spring based energy harvesting from human motions: Design, modeling and experiments. Energy Convers Manag 2017;132:189–97. doi:10.1016/J.ENCONMAN.2016.11.026.

[18] Granados A. Invariant manifolds and the parameterization method in coupled

energy harvesting piezoelectric oscillators. Phys D Nonlinear Phenom 2017;351–352:14–29. doi:10.1016/j.physd.2017.04.003.

[19] Kim I-H, Jung H-J, Lee BM, Jang S-J. Broadband energy-harvesting using a two degree-of-freedom vibrating body. Appl Phys Lett 2011;98:214102. doi:10.1063/1.3595278.

[20] Zhang A, Sorokin V, Li H. Energy harvesting using a novel autoparametric pendulum absorber-harvester. J Sound Vib 2021;499:116014. doi:10.1016/J.JSV.2021.116014.

[21] Kumar R, Gupta S, Ali SF. Energy harvesting from chaos in base excited double pendulum. Mech Syst Signal Process 2019;124:49–64. doi:10.1016/j.ymssp.2019.01.037.

[22] Pan J, Qin W, Deng W, Zhang P, Zhou Z. Harvesting weak vibration energy by integrating piezoelectric inverted beam and pendulum. Energy 2021;227:120374. doi:10.1016/J.ENERGY.2021.120374.

[23] McInnes CR, Gorman DG, Cartmell MP. Enhanced vibrational energy harvesting using nonlinear stochastic resonance. J Sound Vib 2008;318:655–62. doi:10.1016/J.JSV.2008.07.017.

[24] Margielewicz J, Gąska D, Litak G, Wolszczak P, Yurchenko D. Nonlinear dynamics of a new energy harvesting system with quasi-zero stiffness. Appl Energy 2022;307:118159. doi:10.1016/J.APENERGY.2021.118159.

[25] Litak G, Margielewicz J, Gąska D, Wolszczak P, Zhou S. Multiple Solutions of the Tristable Energy Harvester. Energies 2021;14:1284. doi:10.3390/en14051284.

[26] Roca L de la, Peterson J, Pereira M, Cunha AJ. Control of chaos via OGY method on a bistable energy harvester. 25th ABCM Int. Congr. Mech. Eng. (COBEM 2019), 2019.

[27] Zhang Y, Ding C, Wang J, Cao J. High-energy orbit sliding mode control for nonlinear energy harvesting. Nonlinear Dyn 2021 1051 2021;105:191–211. doi:10.1007/S11071-021-06616-8.

[28] Huang Y, Zhao Z, Liu W. Systematic adjustment strategy of a nonlinear beam generator for high-energy orbit. Mech Syst Signal Process 2022;166:108444. doi:10.1016/J.YMSSP.2021.108444.

[29] Yan L, Lallart M, Karami A. Low-cost orbit jump in nonlinear energy harvesters through energy-efficient stiffness modulation. Sensors Actuators A Phys 2019;285:676–84. doi:10.1016/J.SNA.2018.12.009.

[30] Wang J, Liao WH, Cao J. Power enhancement of a monostable energy harvester by orbit jumps: J Intell Mater Syst Struct 2021;32:2601–14. doi:10.1177/1045389X211006912.

[31] Huang Y, Liu W, Yuan Y, Zhang Z. High-energy orbit attainment of a nonlinear beam generator by adjusting the buckling level. Sensors Actuators A Phys 2020;312:112164. doi:10.1016/J.SNA.2020.112164.

[32] Wang J, Liao WH. Attaining the high-energy orbit of nonlinear energy harvesters by load perturbation. Energy Convers Manag 2019;192:30–6. doi:10.1016/J.ENCONMAN.2019.03.075.

[33] Huguet T, Lallart M, Badel A. Orbit jump in bistable energy harvesters through buckling level modification. Mech Syst Signal Process 2019;128:202–15. doi:10.1016/J.YMSSP.2019.03.051.

[34] Margielewicz J, Gąska D, Litak G. Evolution of the geometric structure of strange attractors of a quasi-zero stiffness vibration isolator. Chaos , Solitons Fractals 2019;118:47–57. doi:10.1016/j.chaos.2018.11.012.

[35] Meng Q, Yang X, Li W, Lu E, Sheng L. Research and Analysis of Quasi-Zero-Stiffness

Isolator with Geometric Nonlinear Damping. Shock Vib 2017;2017. doi:10.1155/2017/6719054.

[36] Liu C, Zhao R, Yu K, Lee HP, Liao B. Simultaneous energy harvesting and vibration isolation via quasi-zero-stiffness support and radially distributed piezoelectric cantilever beams. Appl Math Model 2021;100:152–69. doi:10.1016/J.APM.2021.08.002.

[37] Wang K, Zhou J, Ouyang H, Chang Y, Xu D. A dual quasi-zero-stiffness sliding-mode triboelectric nanogenerator for harvesting ultralow-low frequency vibration energy. Mech Syst Signal Process 2021;151:107368. doi:10.1016/J.YMSSP.2020.107368.

[38] Sandri M. Numerical Calculation of Lyapunov Exponents. Math J 1996;6:78–84.

[39] Stefanski A, Dabrowski A, Kapitaniak T. Evaluation of the largest Lyapunov exponent in dynamical systems with time delay. Chaos, Solitons and Fractals 2005;23:1651–9. doi:10.1016/j.chaos.2004.06.051.